Liao *et al. Energy Mater* 2024;4:400025
DOI: 10.20517/energymater.2023.89

Energy Materials

Article

Open Access

Check for updates

Active sites-rich zeolitic imidazolate framework/MXene heterostructure modified separator with improved Li^+ transport for high-performance Li-S batteries

Leiping Liao[1], Huanhuan Duan[1], Guohua Chen[2], Yuanfu Deng[1,3,*]

[1]The Key Laboratory of Fuel Cell for Guangdong Province, School of Chemistry and Chemical Engineering, South China University of Technology, Guangzhou 510640, Guangdong, China.
[2]School of Energy and Environment, City University of Hong Kong, Hong Kong, China.
[3]Guangdong Provincial Research Center of Electrochemical Energy Engineering, South China University of Technology, Guangzhou 510640, Guangdong, China.

***Correspondence to:** Prof. Yuanfu Deng, The Key Laboratory of Fuel Cell for Guangdong Province, School of Chemistry and Chemical Engineering, South China University of Technology, Wushan Road 381, Guangzhou 510640, Guangdong, China. E-mail: chyfdeng@scut.edu.cn

How to cite this article: Liao L, Duan H, Chen G, Deng Y. Active sites-rich zeolitic imidazolate framework/MXene heterostructure modified separator with improved Li^+ transport for high-performance Li-S batteries. *Energy Mater* 2024;4:400025. https://dx.doi.org/10.20517/energymater.2023.89

Received: 6 Nov 2023 **First Decision:** 5 Dec 2023 **Revised:** 21 Dec 2023 **Accepted:** 5 Mar 2024 **Published:** 22 Mar 2024

Academic Editor: Yuping Wu **Copy Editor:** Fanglin Lan **Production Editor:** Fanglin Lan

Abstract

The inevitable shuttling of lithium polysulfides (LiPSs) and poor redox kinetics restrict real-world applications of lithium-sulfur (Li-S) batteries, although they have been paid plentiful attention. Herein, a thin and multifunctional heterostructure (ZIF-L/MXene), consisting of leaf-like zeolitic imidazolate framework sheets (ZIF-L) and two-dimensional layered $Ti_3C_2T_x$ MXene nanosheets, is developed for modification of polyolefin-based separators. A good combination of the merits of the ZIF-L and MXene can hinder the restacking of MXene nanosheets and achieve a large specific surface area, thus exposing plentiful active sites for adsorption and catalytic reaction of LiPSs. Taking these obviously synergistic effects, the ZIF-L/MXene heterostructure modified separators not only alleviate the shuttling of LiPSs but also promote their kinetics conversion. Furthermore, with an improved electrolyte affinity, the ZIF-L/MXene modified separators can accelerate the transport of Li^+. Thus, the modified separator endows a Li-S cell with an admirable discharge capacity of 1371.7 mAh g^{-1} at 0.2 C and favorable cycling stability, with a slow capacity decay ratio of 0.075% per cycle during 500 cycles. Even under a sulfur loading of ~ 4.1 mg cm^{-2}, the Li-S battery can achieve an excellent capacity of 990.6 mAh g^{-1} at 0.1 C and maintain an excellent

cycling performance. The novel ZIF-L/MXene heterostructure modified separator in this work can provide an alternative strategy for designing thin and light separators for high-performance Li-S batteries, via the enhancement of redox kinetics and reduction of shuttling of the LiPSs.

Keywords: Li-S batteries, zeolitic imidazolate framework, MXene, separators, synergistic effects

INTRODUCTION

A great deal of attention was concentrated on developing promising energy storage devices to satisfy the rapidly enhanced demand for high energy density. Lithium-sulfur (Li-S) batteries, which possess the merits of superb energy density (~ 2600 Wh kg^{-1}), environmental friendliness, and low cost, are one kind of potential next-generation batteries[1-3]. Nevertheless, their real-world application is limited by the challenging issues, mainly containing poor conductivity of active material and discharge product, the notorious shuttling of lithium polysulfides (LiPSs), and poor redox kinetics[4-6]. Consequently, the electrochemical performances (such as rate performance and cycling lifetime) of Li-S batteries suffer from a certain degree of damage[7,8].

Various measures have been taken to tackle the aforementioned issues, with attention toward innovative hybrid sulfur hosts[9], optimizing electrolytes[10], and modifying separators[11]. During the past few years, designing a functional separator has been considered a very effective way to alleviate the shuttle effect and facilitate the redox kinetics[12]. Among them, polar materials are extensively employed for the modification of polyolefin separators due to their strong chemical adsorption capacity[13]. However, it is hard to relieve the shuttle effect continuously and efficiently via chemical adsorption. For inhibiting the shuttling of soluble LiPSs at the root, materials with electrocatalytic effects on the conversion reaction of LiPSs are used for functional separators, such as transition metal sulfides[14], transition metal nitrides[15,16], MXenes[17], and metal-organic frameworks (MOFs)[18]. MOFs possess catalytic metal centers and organic ligands with strong LiPSs adsorption capacity to immobilize LiPSs and facilitate their transformation[19]. In particular, as a new star of MOFs, leaf-like Co-containing zeolitic imidazolate frameworks (ZIF-L) with a thickness of a few hundred nanometers and a large specific surface area (SSA) are expected to show massive active sites for alleviating the shuttle effect, thus boosting electrochemical performances of Li-S batteries[20]. Nevertheless, MOFs suffer from poor electrical conductivity, which can easily give rise to poor sulfur utilization and damage the electrochemical performances when they are used as modified materials alone[21].

Two-dimensional (2D) laminar MXenes have drawn massive interest in Li-S batteries on account of their metallic conductivity, intensive polar sites, and catalytic activity[22,23]. Typically, MXenes derived from their parental MAX phases are obtained by selectively removing the A layers, where "M" is assigned to the transition metal, "A" corresponds to the IIIA or IVA elements, "X" is carbon or/and nitrogen, and T_x represents the terminations[24,25]. The sulfophilic surface terminations and conductive Ti-C-Ti bonds can vigorously anchor LiPSs and accelerate the charge transfer kinetics, promoting the utilization of sulfur and thus optimizing the electrochemical performances of Li-S batteries[26]. For instance, Song *et al.* designed a $Ti_3C_2T_x$ MXene modified separator with a thin modified layer of only 522 nm for Li-S batteries[27]. The modified separator endowed the Li-S cell with a discharge capacity of 1046.9 mAh g^{-1} at 0.2 C and maintained a capacity of 743.7 mAh g^{-1} at 1.0 C due to its high conductivity and effective confinement of LiPSs. However, the van der Waals and hydrogen bonding forces lead to serious restacking of MXene nanosheets, thus reducing the number of exposed active sites and limiting catalytic activity[28]. Jiao *et al.* thus rationally designed TiO_2-MXene heterostructures as the multifunctional catalyst of Li-S batteries[29]. The uniformly distributed TiO_2 on MXene nanosheets not only acted as a barrier for inhibiting the restacking of

MXene layers but also played a role in capturing LiPSs. With improved adsorption and catalysis toward the LiPSs, the TiO_2-MXene heterostructure functionalized separator endowed the Li-S cell with a good rate and stable cycle performance. Ren *et al.* reported a heterostructure (CPNC) consisting of CoP and Ti_3C_2, in which the ingenious design alleviates the aggregation of CoP nanocages and restacking of Ti_3C_2 nanosheets, thus revealing plentiful active sites and facilitating the reaction kinetics of sulfur[30]. Consequently, the Li-S cell utilized the Ti_3C_2/CPNC modified separator obtained excellent cycling stability. Tian *et al.* designed a modified separator consisting of carbon nanotubes (CNTs) and MXene@CoS_2 (MCCoS) for Li-S batteries[31]. The CNTs were introduced to expose more active regions for LiPSs catalysis and boost the transport of Li^+ because the size of CoS_2 was too small to hinder the stacking of MXene layers. Profiting from the bifunctional adsorption and catalysis toward LiPSs, the MCCoS/polypropylene (PP) separator helps the Li-S cell realize a rate performance of 368.6 mAh g^{-1} at 20 C and superb cycling performance. Consequently, the rational structural design of MXene hybrids to reveal more active sites is considered a promising strategy for their efficient utilization in Li-S batteries.

Motivated by the above research, to expand the active sites for catalysis conversion sulfur-based species and adsorb more LiPSs, in this work, we first prepared a novel ZIF-L/MXene heterostructure by *in situ* growing the ZIF-L with abundant active metal sites on a conductive MXene. Then, the commercial PP separator was coated with the as-prepared ZIF-L/MXene heterostructure via a simple vacuum filtration process to achieve a modified separator for Li-S batteries. The MXene nanosheets in the ZIF-L/MXene heterostructure not only played the role of a conductive substrate to offer electrons for ZIF-L but also captured LiPSs through the formation of Ti-S bonds and accelerated the conversion of LiPSs. Moreover, the ZIF-L with a large SSA and sufficient active sites could relieve the stacking of MXene layers to expose more active sites and provide a powerful catalytic effect toward LiPSs. Also, the improved electrolyte affinity of the ZIF-L/MXene@PP is in favor of the permeation of electrolytes and the diffusion of Li^+. Profiting from the above many merits, the ZIF-L/MXene modified PP (ZIF-L/MXene@PP) separator indeed endows the Ketjen Black/sulfur (KB/S) cathode with a favorable initial capacity of 1371.7 mAh g^{-1} at 0.2 C and decay rate of 0.075% per cycle during 500 cycles. Besides, the Li-S cell assembled by the KB/S cathode and ZIF-L/MXene@PP separator achieved an excellent capacity of 990.6 mAh g^{-1} at 0.1 C and good cycling stability under the sulfur loading of ~ 4.1 mg cm^{-2} in a low ratio of electrolyte to sulfur (E/S).

RESULTS AND DISCUSSION

The synthesis procedures of the ZIF-L/MXene heterostructure are shown in Figure 1A. Firstly, MXene with a lamellar morphology and plentiful terminations (-OH, -O, and -F) was obtained by removing the Al layer of Ti_3AlC_2 in a mixed aqueous solution containing LiF and HCl[32]. The mild synthesis route makes it easy to obtain MXene nanosheets with large lateral dimensions, which is conducive to the subsequently uniform loading of zeolitic imidazolate frameworks (ZIFs)[33]. The fluorine-containing etching method inevitably leads to a mass of surface terminations with negatively charged surfaces, which easily anchors metal cations. Subsequently, to uniformly obtain the ZIF-L/MXene heterostructure, $Co(NO_3)_2{\cdot}6H_2O$ and 2-methylimidazole (2-MI) dispersed in deionized (DI) water were introduced into the MXene nanosheets aqueous suspension with continuous stirring. Taking advantage of the negatively charged terminations of the MXene nanosheets, the leaf-like ZIFs can be *in situ* grown on MXene under room temperature (RT) through a coprecipitation reaction. After washing with DI water and drying in a vacuum, the leaf-like ZIFs could be conveniently achieved. Herein, by cross-linking with the surface terminations of MXene nanosheets, the Co^{2+} could play a role of nucleation sites for the *in situ* growth of ZIF-L on MXene nanosheets and withstand the electrostatic repulsion between the nanosheets[34].

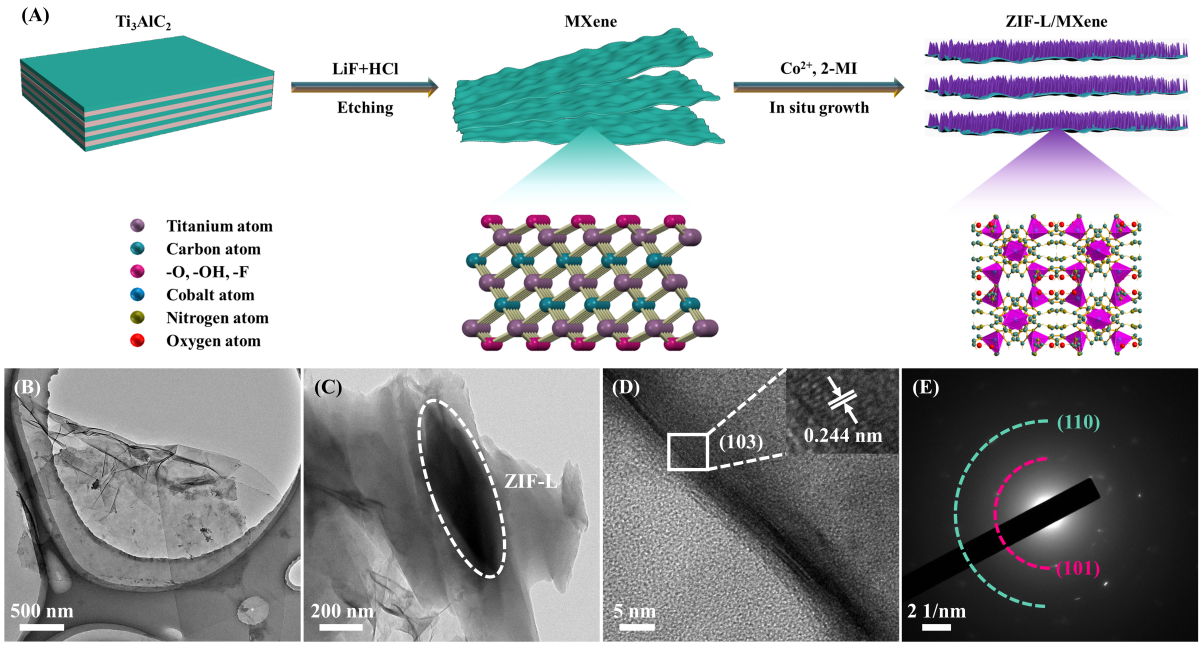

Figure 1. (A) Schematic illustration for the synthesis of the ZIF-L/MXene heterostructure. TEM images of the (B) MXene nanosheets and (C) ZIF-L/MXene heterostructure. (D) HRTEM image and (E) Selected area electron diffraction pattern of the ZIF-L/MXene heterostructure.

To analyze the morphologies and microstructures of the samples, transmission electron microscopy (TEM) was carried out. The TEM image displayed in Figure 1B indicated that the achieved MXene nanosheets had ultrathin thickness and large lateral dimensions. As shown in Figure 1C, the leaf-like ZIFs were successfully grown on MXene nanosheets. A high-resolution TEM (HRTEM) image shown in Figure 1D exhibits a 0.244 nm lattice spacing associated with the (103) crystal plane of MXene. As displayed in Figure 1E, the diffraction rings can be designated to the (101) and (110) crystal planes of MXene. All results demonstrated the successful synthesis of the ZIF-L/MXene heterostructure. The N_2 adsorption-desorption isotherms of the MXene nanosheets and ZIF-L/MXene heterostructure are shown in Supplementary Figure 1, which indicates they are both IV isotherms. The SSAs of the MXene and ZIF-L/MXene are respective of 2.9 and 49.9 m^2/g; the smaller SSA of the MXene can attributed to the restacking of MXene nanosheets resulting from their Vander Waals force between the different layers. In contrast, the larger SSA of the ZIF-L/MXene benefits from the addition of ZIF-L with a high SSA and its positive effect for hindering the stacking of MXene nanosheets. Furthermore, the good combination of the ZIF-L and MXene is beneficial to exposing more active sites for enhancing the interaction with LiPSs when it was employed as a modified layer for Li-S batteries. As displayed in Supplementary Figure 1B and C, the pore distribution curves exhibited that the pore sizes of the ZIF-L/MXene and MXene are mainly distributed in the mesoporous range and the corresponding total pore volumes are 0.075 and 0.017 cm^3/g, respectively. The abundant mesoporous pores are in favor of electrolyte penetration and Li^+ transport. Taking the above-discussed advantages of the ZIF-L/MXene heterostructure, it indicates enormous potential for separator modification in Li-S batteries.

The powder X-ray diffraction (XRD) patterns of MXene and ZIF-L/MXene are displayed in Figure 2A. The disappeared typical (104) peak of Ti_3AlC_2 and the downshift characteristic (002) peak demonstrated the successful removal of Al layers and the formation of MXene nanosheets. The XRD pattern of ZIF-L in the ZIF-L/MXene heterostructure is very similar to its reported simulated pattern, indicating it has the same framework type[35]. Additionally, compared with the MXene, the (002) peak attributed to the MXene in the

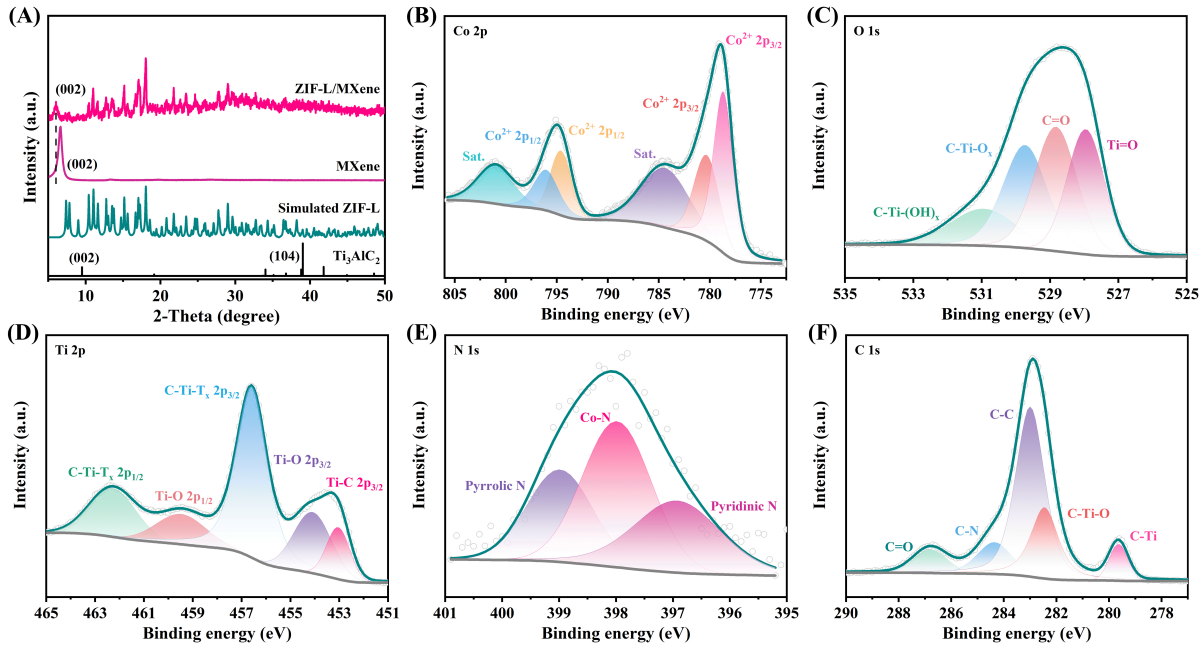

Figure 2. (A) XRD patterns of MXene and ZIF-L/MXene. The high-resolution XPS spectra of (B) Co 2p, (C) O 1s, (D) Ti 2p, (E) N 1s, and (F) C 1s of ZIF-L/MXene.

ZIF-L/MXene heterostructure further downshifts from 6.57° to 5.94°, indicating an expansion in interlayer spacing. The chemical compositions and the corresponding valence state of the corresponding elements of ZIF-L/MXene were characterized by X-ray photoelectron spectroscopy (XPS). The Co 2p and N 1s peaks displayed in Supplementary Figure 2 derived from ZIF-L are displayed in the XPS survey spectrum of ZIF-L/MXene. As displayed in Figure 2B, the peaks at 796.04 and 794.58 eV can ascribed to Co $2p_{1/2}$. The two peaks at 780.30 and 778.67 eV correspond to Co $2p_{3/2}$. Co^{2+} is the main existing form in the ZIF-L/MXene because the energy gaps between Co 2p main peaks and satellites are around 6.0 eV, which are related to Co^{2+}[34,36]. The peaks at 800.98 and 784.37 eV are attributed to the shakeup satellites. The XPS spectrum of O 1s [Figure 2C] includes the peaks of C-Ti-$(OH)_x$ at 530.95 eV, C-Ti-O_x at 529.73 eV, C=O at 528.83 eV, and Ti=O at 527.95 eV, respectively[34,37]. The peaks shown in Figure 2D, which are located at 462.27 and 459.47 eV, belong to C-Ti-T_x and Ti-O of $2p_{1/2}$, respectively [23,38]. The peaks of Ti $2p_{3/2}$ located at 456.58, 454.09, and 453.04 eV match to C-Ti-T_x, Ti-O, and Ti-C, respectively[38-40]. The deconvoluted N 1s spectrum [Figure 2E] reveals pyrrolic nitrogen, Co-N, and pyridinic nitrogen configurations with peaks at 398.98, 397.98, and 396.92 eV, respectively[41]. The spectrum of C 1s displayed in Figure 2F can be deconvoluted into five components located at 286.79, 284.36, 283.00, 282.45, and 279.64 eV are ascribed to C=O, C-N, C-C, C-Ti-O, and C-Ti, respectively[37,42,43]. The XPS results further demonstrate the successful growth of ZIF-L on MXene.

To further explore the possibilities of the as-prepared modified materials for Li-S batteries, the modified materials were coated on PP separators by vacuum filtration. The cross-sectional SEM image of the ZIF-L/MXene@PP separator is indicated in Supplementary Figure 3, in which the thickness of the modification layer onto the PP separator is only 3.3 μm. The ultra-thin modification layer is conducive to reducing unnecessary mass/volume gain and realizing high energy density. Additionally, the SEM and the corresponding element mapping images of the ZIF-L/MXene@PP separator displayed in Supplementary Figure 4 indicate that the C, N, O, Co, and Ti elements uniformly distribute onto the ZIF-L/MXene heterostructure. The top-view SEM images displaying the morphologies of the PP, MXene nanosheets

modified PP (MXene@PP), and ZIF-L/MXene@PP separators were shown in Figure 3A-C, respectively. Compared with a mass of macropores for the PP separator, the macropores of the MXene@PP and ZIF-L/MXene@PP separators were fully covered by the uniform MXene nanosheets and ZIF-L/MXene heterostructure, respectively. The PP separator with plentiful macropores found it hard to efficiently hinder the shuttling of LiPSs, thus causing poor electrochemical performances. In contrast, the MXene@PP and ZIF-L/MXene@PP separators with abundant active sites distributed in the functional layers could immobilize LiPSs and facilitate their conversion. Moreover, the ZIF-L/MXene@PP separator possesses a relatively loose and porous structure than the MXene@PP separator, which naturally leads to faster transport of Li^+. The wettability of the PP, MXene@PP, and ZIF-L/MXene@PP separators toward the electrolyte was revealed by their corresponding contact angle, respectively. Figure 3D indicates that the contact angle of the original PP separator is 37.6°, indicating that the PP separator can be moderately wetted by the electrolyte. The low contact angle of the MXene@PP (7.6°) separator demonstrates that it possesses a higher infiltration capability toward the electrolyte [Figure 3E]. In contrast to the partly wettability of the PP and MXene@PP separators, the contact angle of the ZIF-L/MXene@PP separator shown in Figure 3F is as low as 0°, demonstrating complete wettability. The admirable wettability of the ZIF-L/MXene@PP separator is attributed to the strong polarity of the ZIF-L/MXene heterostructure, which is conducive to the permeation of electrolyte and diffusion of Li^+, thus optimizing the electrochemical performances. To investigate the physicochemical barrier and adsorption ability of the PP and ZIF-L/MXene@PP separators toward Li_2S_6, many permeation tests were performed with the H-type electrolytic cells. The Li_2S_6 infiltrate from Li_2S_6 solution to blank solution with the PP and ZIF-L/MXene@PP separators during 8 h is displayed in Figure 3G. After 8 h, the color of the right bottle changes to yellow, suggesting it is hard for the PP separator to resist the permeation of Li_2S_6. For the device with the ZIF-L/MXene@PP separator, there is nearly no color change on the right bottle, demonstrating an excellent adsorption effect towards Li_2S_6, which is mainly attributed to the high SSA and exposed sulfurophilic active sites.

To further investigate the LiPSs adsorption capacity of these modified materials, MXene and ZIF-L/MXene of the same mass were added into 2 mM Li_2S_6 solution for standing for 6 h. Also, the blank Li_2S_6 solution was standing at the same time for comparison. As shown in Figure 4A, there was no change in the color for the blank Li_2S_6 solution, but the solution containing MXene became lighter, indicating that MXene can effectively adsorb Li_2S_6. In contrast, the Li_2S_6 solution containing ZIF-L/MXene turned almost colorless, demonstrating a better adsorption effect on Li_2S_6. The ultraviolet-visible (UV-vis) spectrum of the blank Li_2S_6 solution displays a characteristic peak at around 275 nm, which contributes to the S_6^{2-} species[44]. After adsorption by the MXene and ZIF-L/MXene heterostructure, the intensity of the S_6^{2-} peak both decreased. Furthermore, the peak intensity from the supernatant in the bottle containing the ZIF-L/MXene heterostructure is the weakest, indicating the lowest concentration of Li_2S_6 and the best adsorption capacity toward LiPSs.

The redox kinetics of soluble LiPSs is critical to hindering the shuttling of LiPSs and optimizing electrochemical performances[45]. To investigate the catalytic ability of the modified materials on LiPSs, symmetric cells were assembled by the identical MXene electrode or ZIF-L/MXene electrode with 0.2 M Li_2S_6 electrolyte, and the CV measurements were carried out using the assembled symmetric cells between the potential window -1.5 to 1.5 V. Also, the CV curve of the ZIF-L/MXene electrode in electrolyte without Li_2S_6 was utilized for comparison to eliminate the capacitive contribution. As shown in Figure 4B, the lowest current density was observed in the battery assembled by the ZIF-L/MXene electrode without the addition of Li_2S_6, which demonstrated that the lithiation/delithiation reactions were the major contribution to current response[46]. Specifically, the ZIF-L/MXene-based symmetric cell with Li_2S_6 electrolyte exhibited a larger current density and smaller polarization potential than that of the MXene-based symmetric cell at

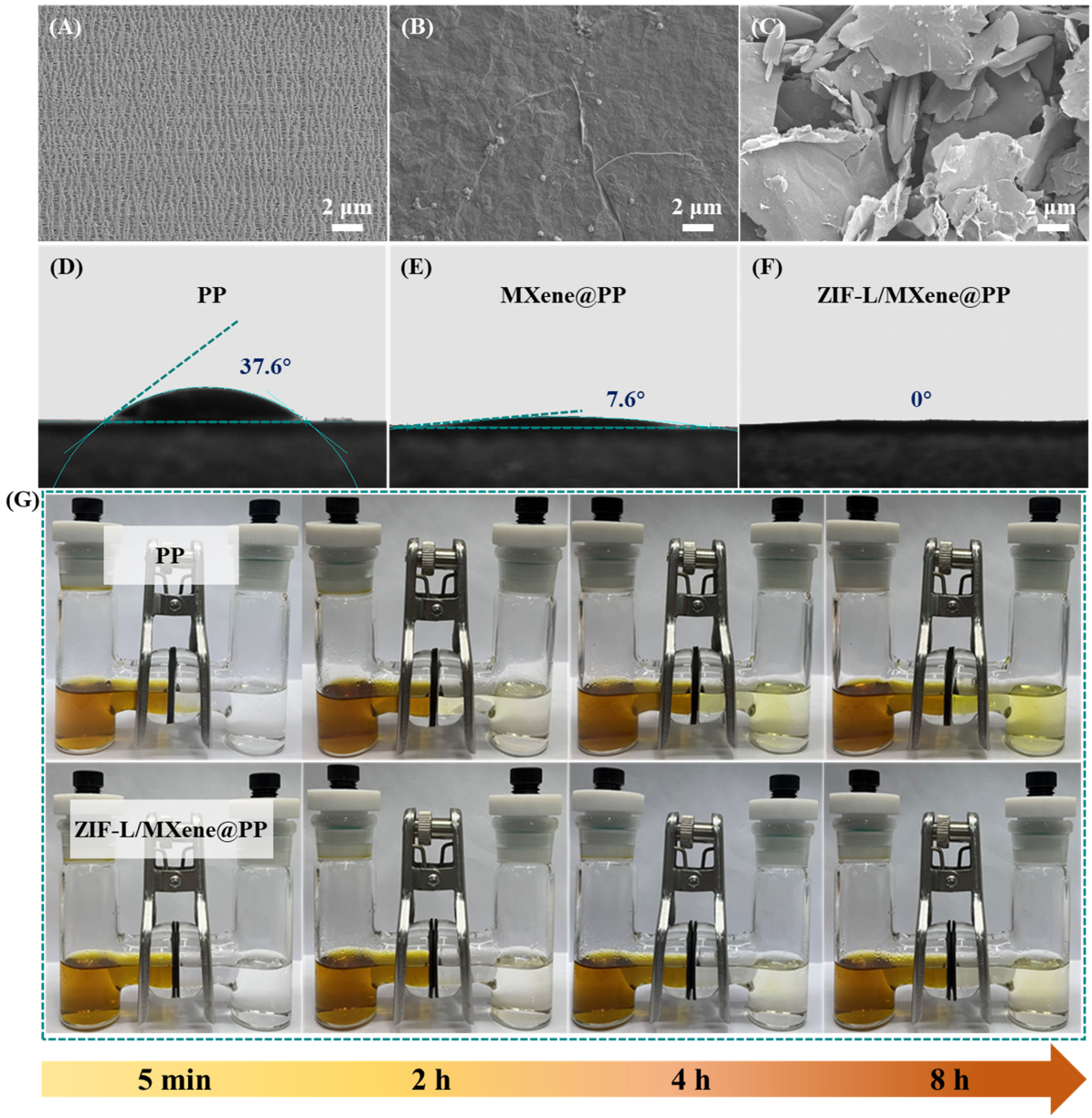

Figure 3. (A-C) Top-view SEM images of the PP, MXene@PP, and ZIF-L/MXene@PP separators. (D-F) The contact angle tests between electrolyte and PP, MXene@PP, or ZIF-L/MXene@PP separators. (G) Li_2S_6 permeation measurements of the PP and ZIF-L/MXene@PP separators.

10 mV s^{-1}, respectively, indicating a better catalytic ability on the conversion of Li_2S_6 and less barrier for ions migration. Generally, this catalytic behavior is conducive to efficiently utilizing active sulfur-based species at a high rate for Li-S cells. Additionally, the redox current of the ZIF-L/MXene-based symmetric cell was greatly improved, and there was no obvious change after five cycles at 1000 mV s^{-1} [Supplementary Figure 5], which indicated that the good catalytic effect can be well maintained during the battery cycle. The catalytic activity of the modified materials was further studied by CV curves of Li-S cells. As displayed in Figure 4C, the cathodic peaks I and II correspond to the decrease of solid sulfur into soluble LiPSs and the conversion of soluble LiPSs to Li_2S/Li_2S_2, respectively[46]. The anodic peaks III and IV are associated with the oxidation of Li_2S/Li_2S_2 into soluble LiPSs and the conversion of soluble LiPSs to solid sulfur, respectively[46]. It can be

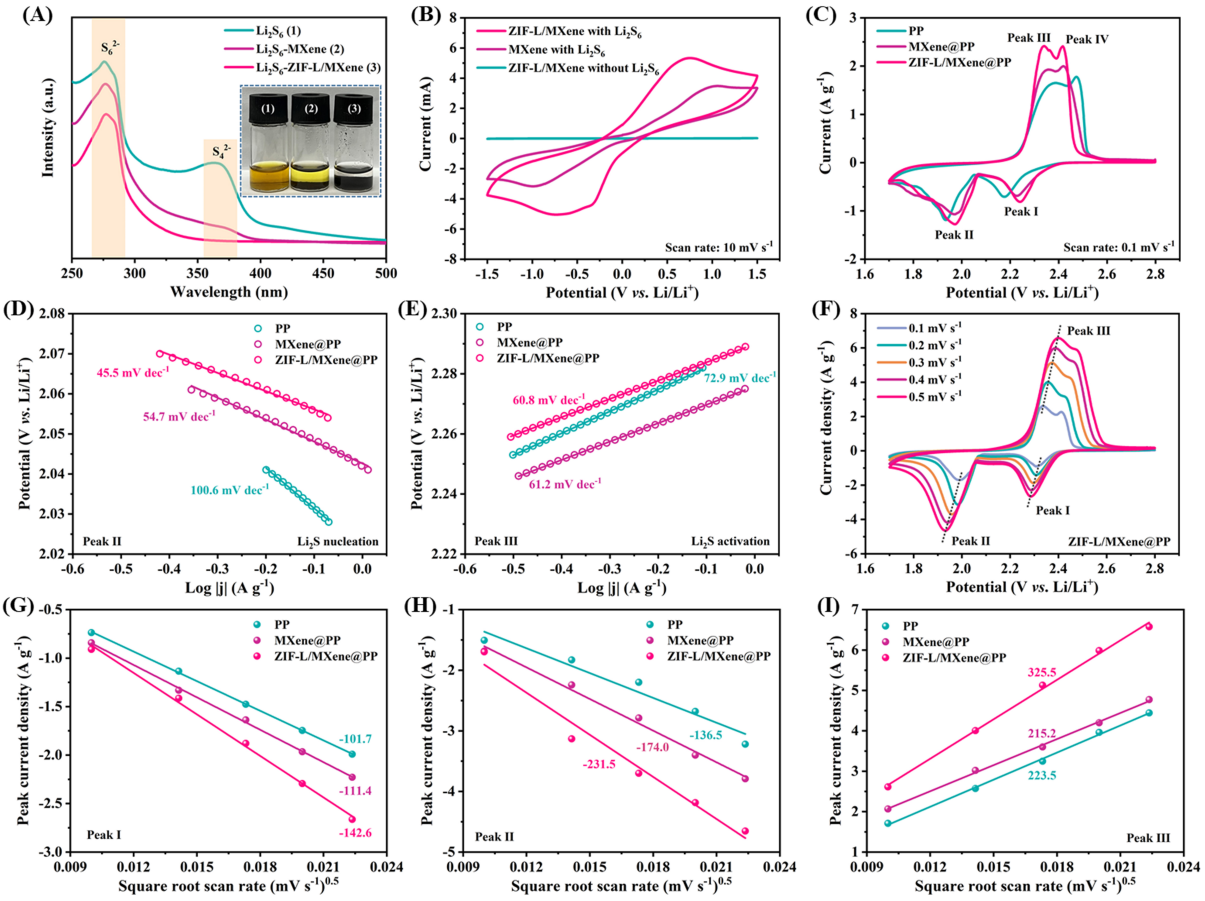

Figure 4. (A) UV-vis spectra of the supernatants (inset: digital images of blank Li_2S_6, Li_2S_6-MXene, and Li_2S_6-ZIF-L/MXene solutions, respectively). (B) CV curves of symmetric cells. (C) The first CV curves of the PP, MXene@PP, and ZIF-L/MXene@PP-based Li-S cells. Tafel plots of the (D) cathodic peak and (E) anodic peak derived from the CV curves. (F) CV curves of ZIF-L/MXene@PP-based Li-S cell at 0.1, 0.2, 0.3, 0.4, and 0.5 mV s^{-1}, respectively. Plots of peak current densities for (G) peak I, (H) peak II, and (I) peak III *vs.* the square root of the scan rate.

observed that the peak current densities of reduction and oxidation peaks of the ZIF-L/MXene@PP-based Li-S cell are obviously higher than those of the MXene@PP and PP-based Li-S cells, respectively, which is beneficial from the improved utilization of sulfur by the ZIF-L/MXene@PP. Furthermore, it is observed that the reduction and oxidation peaks of the ZIF-L/MXene@PP-based Li-S cell shifted to the higher and lower potential, respectively. These results demonstrated that the ZIF-L/MXene can indeed promote the conversion of sulfur-based species in both reduction and oxidation reactions. The Tafel slopes of the reduction and oxidation process in Figure 4D and E show that the fitted slopes follow the order of ZIF-L/MXene@PP<MXene@PP<PP, indicating that the ZIF-L/MXene improved the reaction kinetics of sulfur species[46]. The CV curves [Figure 4F and Supplementary Figure 6] were measured at different scan rates to further investigate the Li^+ diffusion kinetics and reaction kinetics of sulfur species. In general, the Li^+ diffusion efficiency can be evaluated according to the Randles-Sevcik formula[46]:

$$I_p = (2.69\times10^5)\, n^{1.5}\, A D_{Li^+}{}^{0.5}\, C_{Li^+}\, v^{0.5} \quad (1)$$

where I_p signifies the peak current density, n denotes the number of charges transferred, A represents the area of the electrode, D_{Li+} stands for the diffusion coefficient of Li^+, C_{Li+} refers to the concentration of Li^+, and v indicates the scan rate. The D_{Li+} is positively correlated to the absolute value of the slope for the fitted lines shown in Figure 4G-I, among which the ZIF-L/MXene@PP displays the largest absolute value, implying that the ZIF-L/MXene@PP possesses a higher Li^+ diffusion in both oxidation and reduction process in the Li-S cells, respectively, thus boosting the redox reaction of LiPSs[47].

Electrochemical impedance spectroscopy (EIS) was performed at the open-circuit potentials to reveal the enhanced redox kinetics. As displayed in Figure 5A, the intercept between the semicircle and coordinate axis can be denoted as R_1 which is the solution resistance of the electrolyte; the semicircle at high frequency is marked as R_2 which represents the charge transfer resistance, and the sloped line at low frequency is labeled as W_1 which means the Warburg impedance[15]. The R_2 of the PP, MXene@PP, and ZIF-L/MXene@PP-based Li-S cells are 99.56, 72.18, and 70.17 Ω, respectively. The lowest R_2 of the ZIF-L/MXene@PP-based cell can ascribed to the unique structure of ZIF-L/MXene, which conduces to fast charge transfer and Li^+ diffusion[45]. As shown in Supplementary Figure 7, the charge transfer resistances of the Li-S cells were greatly decreased after 100 cycles at 1.0 C, which can be put down to the activation of active materials. The rate performances of PP, MXene@PP, and ZIF-L/MXene@PP-based Li-S cells were measured at the current densities ranging from 0.2 to 2.0 C. Figure 5B and Supplementary Figure 8 demonstrate that the ZIF-L/MXene@PP-based cell achieved specific capacities of 1371.7, 878.5, 797.1, and 710.2 mAh g^{-1} at 0.2, 0.5, 1.0, and 2.0 C, respectively. However, the Li-S cells that employed the MXene@PP, ZIF-L@PP, and PP separators only obtained 1197.6, 1172.2, and 1157.2 mAh g^{-1} at 0.2 C, and 543.0, 535.4, and 517.0 mAh g^{-1} at 2.0 C, respectively. The improved specific capacity of the ZIF-L/MXene@PP-based cell benefits from the large exposed active surface of the ZIF-L/MXene heterostructure with good adsorption and catalysis toward LiPSs. Figure 5C displays the galvanostatic charge/discharge (GCD) curves of the Li-S cells with various modified separators which were tested at 0.2 C. The lowest polarization potential (ΔE) reveals the fastest LiPSs conversion kinetics of the ZIF-L/MXene@PP-based cell[48]. Also, the ratio of the Q_L to Q_H is utilized to evaluate the catalytic effect for boosting the soluble LiPSs change to solid discharge products, among which the Q_L and Q_H represent the low and high discharge plateau, respectively[15]. The results shown in Supplementary Figure 9 demonstrate that the highest value of the Q_L/Q_H for the ZIF-L/MXene@PP-based cell corresponds to the excellent catalytic activity of the ZIF-L/MXene heterostructure. For further investigating the cycling stability, the Li-S cells with various separators were measured at 1.0 C [Figure 5D and Supplementary Figure 8]. The average decay ratio per cycle is 0.075%, 0.099%, 0.111%, and 0.106% for ZIF-L/MXene@PP, MXene@PP, ZIF-L@PP, and PP-based Li-S cells, respectively. Additionally, the ZIF-L/MXene@PP, MXene@PP, ZIF-L@PP, and PP-based Li-S cells indicated Coulombic efficiencies of 96.7%, 95.7%, 90.0%, and 93.2% after 500 cycles, respectively. Owing to the synergistic effect of the ZIF-L and MXene that provided effective suppression of the shuttling of LiPSs, thus achieving favorable cycling performance. As shown in Supplementary Figure 10, the Li-S cell cannot achieve a higher cycling performance with a lighter ZIF-L/MXene modified layer. Furthermore, the electrochemical performance comparisons of the ZIF-L/MXene-PP separator with other functional separators in recent literature were listed in Supplementary Table 1. Under the condition of low E/S ratio (10 μL·mg^{-1}) and high sulfur loading (~ 4.1 mg cm^{-2}), the Li-S cell employed the ZIF-L/MXene@PP also achieved a good initial capacity of 990.6 mAh g^{-1} and maintained 77.2% capacity after 100 cycles and 97.3% Coulombic efficiency [Figure 5E]. The self-discharge behavior is also crucial evidence to evaluate the inhibition of the shuttling of LiPSs, which is generated by the reduction of sulfur species and shuttle effect in the Li-S cells[49]. The open circuit voltages of the Li-S cells are tested with ZIF-L/MXene@PP, MXene@PP, and PP separators, respectively (Figure 5F). The open circuit voltages decreased within a few hours and gradually stabilized over the following time. It is found that the open circuit voltages of the ZIF-L/MXene@PP, MXene@PP, and PP-based Li-S cells were 2.69, 2.49, and 2.41 V for 25 h rest, demonstrating that the modified separators could effectively relieve the

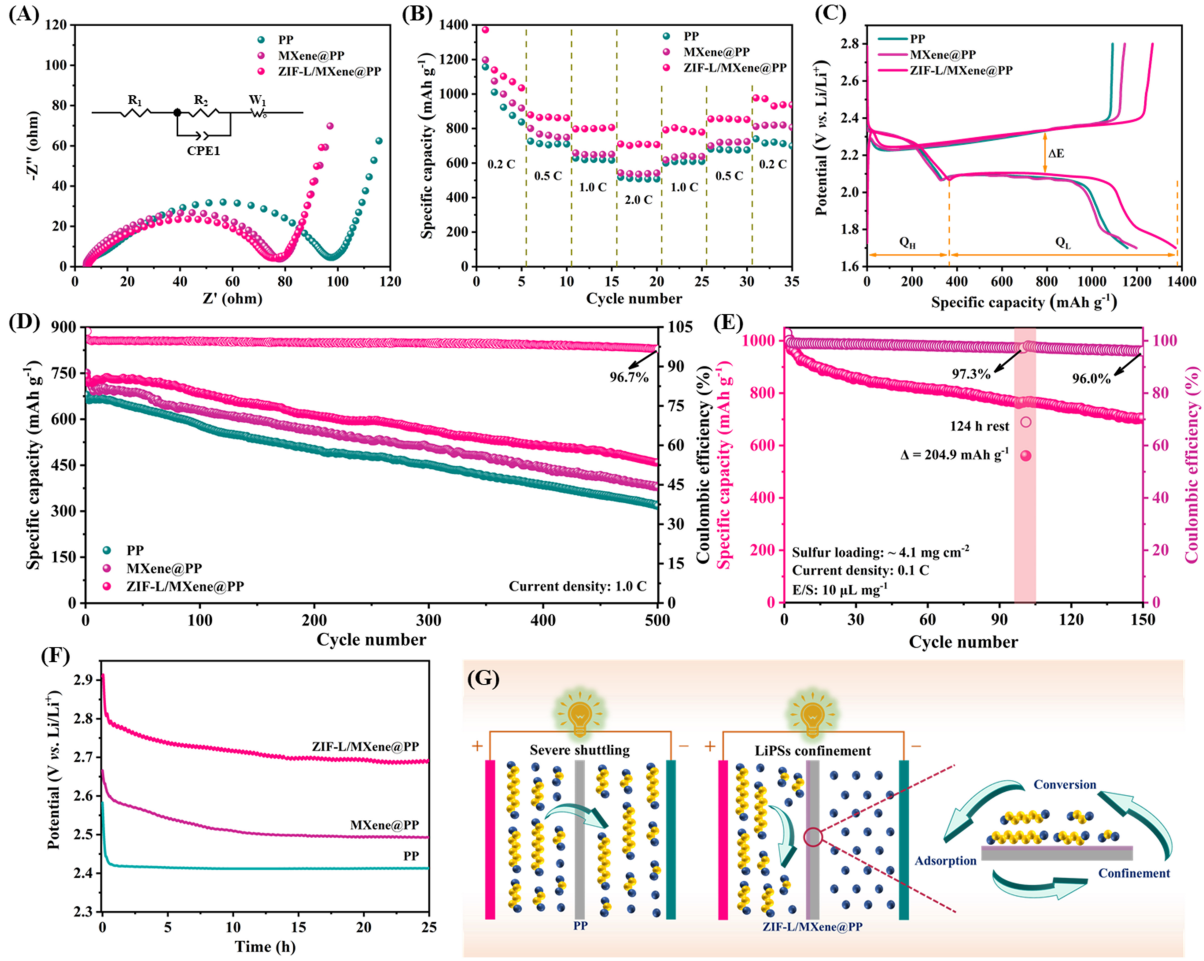

Figure 5. (A) EIS curves of the fresh PP, MXene@PP, and ZIF-L/MXene@PP-based Li-S cells, respectively. (B) Rate performance, (C) the GCD curves measured at 0.2 C, and (D) cycling performances. (E) Cycling performance of the ZIF-L/MXene@PP-based Li-S cell and then rest for 124 h. (F) The open circuit voltages of the PP, MXene@PP, and ZIF-L/MXene@PP-based Li-S cells, respectively. (G) Schematic illustrations of the adsorption and conversion of LiPSs on ZIF-L/MXene@PP.

shuttling of LiPSs and the ZIF-L/MXene@PP separator exhibited a better effect. The self-discharge behavior of the ZIF-L/MXene@PP-based cell was further investigated under the condition of high sulfur loading and low E/S. As displayed in Figure 5E, the ZIF-L/MXene@PP-based cell was cycled for 100 cycles, followed by 124 h rest, and then cycled for 50 cycles. The Li-S cell employed the ZIF-L/MXene@PP-based exhibited a capacity decrease of 204.9 mAh g^{-1} after 124 h rest, but the capacity recovered its condition before rest during the second discharge process after rest, indicating an excellent ability for suppressing the self-discharge using the modified ZIF-L/MXene@PP separator. The schematic illustrations of the adsorption and conversion of LiPSs on ZIF-L/MXene@PP are shown in Figure 5G. Based on the common effect of the MXene and ZIF-L, the LiPSs were anchored on ZIF-L/MXene@PP, followed by rapid conversion to optimize the electrochemical performances of Li-S cells.

To further reveal the impact of modified separators on relieving the shuttling of LiPSs, Li-S cells with various modified separators were cycled at 1.0 C for 300 cycles and then disassembled to characterize the erosion degree of the Li anode. Figure 6A indicates a severely corrosive microstructure on the surface of the Li anode for the PP-based Li-S cell. By contrast, the MXene@PP-based cell displays a flatter and smoother

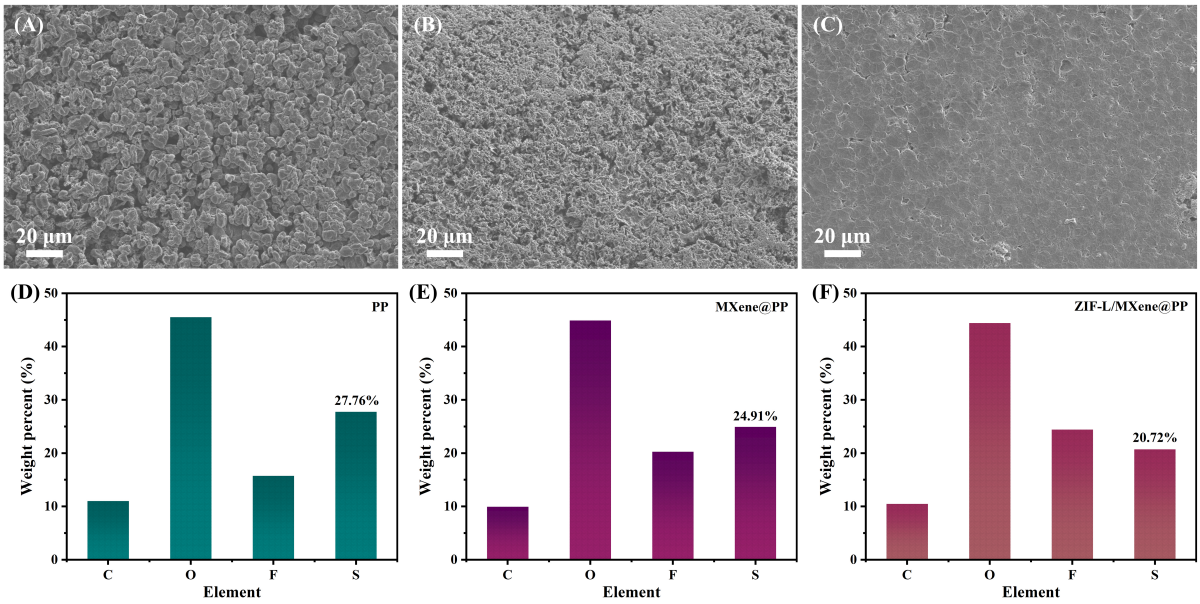

Figure 6. SEM images and corresponding element contents of lithium metal anodes from (A, D) PP, (B, E) MXene@PP, and (C, F) ZIF-L/MXene@PP-based Li-S cells after 300 cycles at 1.0 C.

surface for the Li anode [Figure 6B], indicating an effective effect on inhibiting the shuttling of LiPSs. As shown in Figure 6C, the flattest and smoothest surface of Li foil was realized by the Li-S cell which employed the ZIF-L/MXene@PP separator, demonstrating the most ability of hindering the shuttling of LiPSs. The element content and element mapping images of the surface of Li foils are shown in Figure 6D-F and Supplementary Figures 11-13. The ZIF-L/MXene@PP separator exhibited a more obvious effect on adsorbing and confining LiPSs than PP and MXene@PP separators because the Li foil from the ZIF-L/MXene@PP-based cell exhibits fewer sulfur species on the surface. All results indicated that the ZIF-L/MXene@PP separator with a high LiPSs adsorption and obvious catalytic effect can effectively boost the electrochemical performances of Li-S batteries.

CONCLUSION

In summary, we successfully prepared a thin and multifunctional heterostructure with the leaf-like ZIF-L distributed on 2D MXene nanosheets that possess enhanced LiPSs adsorption and catalytic activity as the functional modified layer of the separator for the Li-S battery. Profiting from the large exposed active sites and improved electrolyte affinity of the ZIF-L/MXene heterostructure, the ZIF-L/MXene@PP separator with a thickness of ~ 3.3 μm for coating layer achieves a superb initial discharge capacity of 1371.7 mAh g^{-1} at 0.2 C, high Coulombic efficiency, and favorable cycling stability for a Li-S battery. Furthermore, the assembled Li-S cell with this modified separator also achieved an excellent initial discharge capacity and long cycling life under high sulfur loading and low E/S ratios. Therefore, the ZIF-L/MXene heterostructure can provide an idea of thin and light design toward a modified layer of separator for high-performance Li-S batteries.

EXPERIMENTAL SECTION

Preparation of the MXene nanosheets

First, 2.0 g of LiF was dissolved in 40 mL of HCl (9.0 M) by stirring for 30 min at 35 ℃ to achieve a homogeneous solution. Ti_3AlC_2 powder (2.0 g) was then slowly added to the mixture. After 36 h, wash the product through the DI water to remove the acid and obtain the neutral solution. Subsequently, the MXene

nanosheets were obtained by repeated shaking and centrifugal treatments.

Fabrication of the ZIF-L/MXene heterostructures

The ZIF-L/MXene heterostructure was synthesized via *in situ* growth at RT. Firstly, 0.1 g of MXene, 0.4 g of $Co(NO_3)_2 \cdot 6H_2O$, and 0.9 g of 2-MI were dispersed in DI water (20 mL), respectively. Subsequently, these solutions were mixed and stirred at RT for 4 h. The ZIF-L/MXene heterostructure was collected after washing with DI water and a vacuum drying process.

Preparation of the ZIF-L/MXene@PP and MXene@PP separators

The modified PP separators were fabricated using a vacuum filtration method. Typically, 20 mg ZIF-L/MXene was dispersed in methanol with sonication under an ice bath. Then, the obtained suspension was vacuum filtered on the PP separator, and the as-prepared ZIF-L/MXene@PP separator was dried at RT over 12 h. Similarly, the MXene@PP separator was fabricated through the same process except the ZIF-L/MXene was replaced by MXene. Finally, cut the ZIF-L/MXene@PP and MXene@PP separators into circular disks that possess diameter and mass loading of 19 mm and ~ 0.13 mg cm^{-2}, respectively.

Visualized Adsorption of Polysulfides

S and Li_2S with a molar ratio of 5:1 were dissolved in a solution of DME/DOL (volume ratio of 1:1) to obtain a 2.0 mM Li_2S_6 solution and then stirred at 60 ℃ for 12 h in an argon-filled glovebox. Additionally, 20 mg of MXene and ZIF-L/MXene were added into 2.0 mL Li_2S_6 solution for comparison, respectively.

Assembly of Li_2S_6 symmetric batteries

Symmetric batteries were assembled with two identical ZIF-L/MXene or MXene electrodes, a Celgard 2500 separator (25 μm), and 40 μL of Li_2S_6 electrolyte. Coating the homogeneous slurry of ZIF-L/MXene and PVDF (mass ratio of 9:1) onto circular carbon-coated Al foils (diameter of 14 mm), then vacuum drying and the mass loading of obtained electrodes were 0.3 mg cm^{-2}. For comparisons, the MXene electrodes were prepared using the same method. Dissolving S and Li_2S with a molar ratio of 5:1 into an electrolyte containing 1.0 M lithium bis (trifluoromethanesulfonyl) imide (LiTFSI) with 2.0 wt% $LiNO_3$ in DME/DOL (volume ratio of 1:1) to achieve 0.2 M Li_2S_6 electrolyte.

Cathode preparation and electrochemical tests

S and KB powder were mixed in ethanol, stirred for 40 min, and dried at 60 °C. Then, the KB/S composite was synthesized through a melt-diffusion process with heat treatment at 210 °C for 12 h in an argon atmosphere. The TGA curve shown in Supplementary Figure 14 suggested that the sulfur content is 75.5%. The as-prepared KB/S composite and PVDF were stirred in NMP with a mass ratio of 9:1 and then coated on circular carbon-coated Al foils (diameter of 14 mm) and dried under vacuum at 60 °C for later use. The S mass loadings of regular cathodes were between 1.2-1.5 mg·cm^{-2} and the high loading was up to ~ 4.1 mg·cm^{-2}.

The CR2016-type coin cells were assembled with pure lithium metal and ZIF-L/MXene@PP as the anodes and separators, respectively. The electrolyte consisted of 1.0 M LiTFSI dissolved in DME/DOL (volume ratio of 1:1) with a 2.0 wt% $LiNO_3$ additive. The ratio of E/S was 20 and 10 μL·mg^{-1} for the conventional and high-sulfur-loading electrodes, respectively. The GCD tests were measured on a multichannel battery test system (Neware CT-3008W) between 1.7 to 2.8 V. CV measurements were all performed on an electrochemical workstation (CHI660D), and the EIS was tested from 0.01 Hz to 100 kHz.

DECLARATIONS

Authors' contributions

Methodology, characterization, data analysis, writing-original draft: Liao L
Data analysis, writing-review: Duan H
Writing-review & editing: Chen G
Conceptualization, supervision, writing-review & editing, funding resources: Deng Y
All authors have given approval to the final version of the manuscript.

Availability of data and materials

All data are available in the manuscript and the Supplementary Material.

Financial support and sponsorship

This work was supported by the National Natural Science Foundation of China-Hong Kong Research Grant Council (NSFC-RGC) Joint Research Scheme (Grant No. 21661162002 and N_HKUST601/16). We also thank the National Natural Science Foundation of China (Grant Nos. 21875071 and 22178125) for providing financial support.

Conflicts of interest

All authors declared that there are no conflicts of interest.

Ethical approval and consent to participate

Not applicable.

Consent for publication

Not applicable.

REFERENCES

1. Chen ZX, Cheng Q, Li XY, et al. Cathode kinetics evaluation in lean-electrolyte lithium-sulfur batteries. *J Am Chem Soc* 2023;145:16449-57. DOI
2. Wang X, Luo D, Wang J, et al. Strain engineering of a MXene/CNT hierarchical porous hollow microsphere electrocatalyst for a high-efficiency lithium polysulfide conversion process. *Angew Chem Int Ed Engl* 2021;60:2371-8. DOI
3. Wang T, Luo D, Zhang Y, et al. Hierarchically porous Ti_3C_2 MXene with tunable active edges and unsaturated coordination bonds for superior lithium-sulfur batteries. *ACS Nano* 2021;15:19457-67. DOI
4. Zhang Y, Kang C, Zhao W, et al. d-p Hybridization-induced "trapping-coupling-conversion" enables high-efficiency Nb single-atom catalysis for Li-S batteries. *J Am Chem Soc* 2023;145:1728-39. DOI
5. Ding X, Yang S, Zhou S, et al. Biomimetic molecule catalysts to promote the conversion of polysulfides for advanced lithium-sulfur batteries. *Adv Funct Materials* 2020;30:2003354. DOI
6. Li X, Guan Q, Zhuang Z, et al. Ordered mesoporous carbon grafted MXene catalytic heterostructure as Li-ion kinetic pump toward high-efficient sulfur/sulfide conversions for Li-S battery. *ACS Nano* 2023;15:1653-62. DOI
7. Li Z, Sun Y, Wu X, Yuan H, Yu Y, Tan Y. Boosting adsorption and catalysis of polysulfides by multifunctional separator for lithium-sulfur batteries. *ACS Energy Lett* 2022;7:4190-7. DOI
8. Li Y, Deng Y, Yang J, Tang W, Ge B, Liu R. Bidirectional catalyst with robust lithiophilicity and sulfiphilicity for advanced lithium-sulfur battery. *Adv Funct Materials* 2023;33:2302267. DOI
9. Sun X, Qiu Y, Jiang B, et al. Isolated Fe-Co heteronuclear diatomic sites as efficient bifunctional catalysts for high-performance lithium-sulfur batteries. *Nat Commun* 2023;14:291. DOI PubMed PMC
10. Zhao M, Li B, Chen X, Xie J, Yuan H, Huang J. Redox comediation with organopolysulfides in working lithium-sulfur batteries. *Chem* 2020;6:3297-311. DOI
11. Li L, Tu H, Wang J, et al. Electrocatalytic MOF-carbon bridged network accelerates Li^+-solvents desolvation for high Li^+ diffusion toward rapid sulfur redox kinetics. *Adv Funct Materials* 2023;33:2212499. DOI

12. Wang M, Zhu Y, Sun Y, et al. A universal graphene-selenide heterostructured reservoir with elevated polysulfide evolution efficiency for pragmatic Lithium-Sulfur Battery. *Adv Funct Materials* 2023;33:2211978. DOI
13. He J, Chen Y, Manthiram A. Vertical Co9S8 hollow nanowall arrays grown on a Celgard separator as a multifunctional polysulfide barrier for high-performance Li-S batteries. *Energy Environ Sci* 2018;11:2560-8. DOI
14. Wang S, Chen H, Liao J, et al. Efficient trapping and catalytic conversion of polysulfides by VS4 nanosites for Li-S batteries. *ACS Energy Lett* 2019;4:755-62. DOI
15. Xia J, Hua W, Wang L, et al. Boosting catalytic activity by seeding nanocatalysts onto interlayers to inhibit polysulfide shuttling in Li-S batteries. *Adv Funct Materials* 2021;31:2101980. DOI
16. Lai C, Zhou X, Lei M, Liu W, Mu X, Li C. Scissor g-C_3N_4 for high-density loading of catalyst domains in mesoporous thin-layer conductive network for durable Li-S batteries. *Energy Mater* 2023;3:300025. DOI
17. Chen L, Sun Y, Wei X, et al. Dual-functional V_2C MXene assembly in facilitating sulfur evolution kinetics and Li-ion sieving toward practical lithium-sulfur batteries. *Adv Mater* 2023;35:e2300771. DOI
18. Chen Y, Zhang L, Pan H, et al. Pore-space-partitioned MOF separator promotes high-sulfur-loading Li-S batteries with intensified rate capability and cycling life. *J Mater Chem A* 2021;9:26929-38. DOI
19. Hu X, Huang T, Zhang G, et al. Metal-organic framework-based catalysts for lithium-sulfur batteries. *Coord Chem Rev* 2023;475:214879. DOI
20. Wu G, Sun S, Zhu X, Ma Z, Zhang Y, Bao N. Microfluidic fabrication of hierarchical-ordered ZIF-L(Zn)@Ti_3C_2Tx core-sheath fibers for high-performance asymmetric supercapacitors. *Angew Chem Int Ed Engl* 2022;61:e202115559. DOI
21. Wang L, Feng X, Ren L, et al. Flexible solid-state supercapacitor based on a metal-organic framework interwoven by electrochemically-deposited PANI. *J Am Chem Soc* 2015;137:4920-3. DOI
22. Song Y, Sun Z, Fan Z, et al. Rational design of porous nitrogen-doped Ti_3C_2 MXene as a multifunctional electrocatalyst for Li-S chemistry. *Nano Energy* 2020;70:104555. DOI
23. Li P, Lv H, Li Z, et al. The electrostatic attraction and catalytic effect enabled by ionic-covalent organic nanosheets on MXene for separator modification of lithium-sulfur batteries. *Adv Mater* 2021;33:e2007803. DOI
24. Naguib M, Barsoum MW, Gogotsi Y. Ten years of progress in the synthesis and development of MXenes. *Adv Mater* 2021;33:e2103393. DOI PubMed
25. Zhao Q, Zhu Q, Liu Y, Xu B. Status and prospects of MXene-based lithium-sulfur batteries. *Adv Funct Materials* 2021;31:2100457. DOI
26. C(, Cui L, Abdolhosseinzadeh S, Heier J. Two-dimensional MXenes for lithium-sulfur batteries. *InfoMat* 2020;2:613-38. DOI
27. Song J, Su D, Xie X, et al. Immobilizing polysulfides with MXene-functionalized separators for stable lithium-sulfur batteries. *ACS Appl Mater Interfaces* 2016;8:29427-33. DOI
28. Zhao Y, Zhang J, Guo X, et al. Engineering strategies and active site identification of MXene-based catalysts for electrochemical conversion reactions. *Chem Soc Rev* 2023;52:3215-64. DOI
29. Jiao L, Zhang C, Geng C, et al. Capture and catalytic conversion of polysulfides by in situ built TiO_2-MXene heterostructures for lithium-sulfur batteries. *Adv Energy Mater* 2019;9:1900219. DOI
30. Ren Y, Wang B, Liu H, et al. CoP nanocages intercalated MXene nanosheets as a bifunctional mediator for suppressing polysulfide shuttling and dendritic growth in lithium-sulfur batteries. *Chem Eng J* 2022;450:138046. DOI
31. Tian S, Zeng Q, Liu G, et al. Multi-dimensional composite frame as bifunctional catalytic medium for ultra-fast charging lithium-sulfur battery. *Nanomicro Lett* 2022;14:196. DOI PubMed PMC
32. Yan J, Ren CE, Maleski K, et al. Flexible MXene/Graphene films for ultrafast supercapacitors with outstanding volumetric capacitance. *Adv Funct Materials* 2017;27:1701264. DOI
33. Ghidiu M, Lukatskaya MR, Zhao MQ, Gogotsi Y, Barsoum MW. Conductive two-dimensional titanium carbide 'clay' with high volumetric capacitance. *Nature* 2014;516:78-81. DOI PubMed
34. Liu C, Bai Y, Li W, Yang F, Zhang G, Pang H. In situ growth of three-dimensional MXene/metal-organic framework composites for high-performance supercapacitors. *Angew Chem Int Ed Engl* 2022;61:e202116282. DOI
35. Chen R, Yao J, Gu Q, et al. A two-dimensional zeolitic imidazolate framework with a cushion-shaped cavity for CO2 adsorption. *Chem Commun (Camb)* 2013;49:9500-2. DOI
36. Qin J, Wang S, Wang X. Visible-light reduction CO_2 with dodecahedral zeolitic imidazolate framework ZIF-67 as an efficient co-catalyst. *Appl Catal B* 2017;209:476-82. DOI
37. Ramírez R, Melillo A, Osella S, Asiri AM, Garcia H, Primo A. Green, HF-free synthesis of MXene quantum dots and their photocatalytic activity for hydrogen evolution. *Small Methods* 2023;7:e2300063. DOI PubMed
38. Gu S, Jiang H, Li X, et al. Dispersing single-layered $Ti_3C_2T_x$ nanosheets in hierarchically-porous membrane for high-efficiency Li^+ transporting and polysulfide anchoring in Li-S batteries. *Energy Stor Mater* 2022;53:32-41. DOI
39. Han X, An L, Hu Y, et al. Ti_3C_2 MXene-derived carbon-doped TiO_2 coupled with g-C_3N_4 as the visible-light photocatalysts for photocatalytic H_2 generation. *Appl Catal B* 2020;265:118539. DOI
40. Feng X, Ning J, Wang B, et al. Functional integrated electromagnetic interference shielding in flexible micro-supercapacitors by cation-intercalation typed $Ti_3C_2T_x$ MXene. *Nano Energy* 2020;72:104741. DOI
41. Song C, Li G, Yang Y, et al. 3D catalytic MOF-based nanocomposite as separator coatings for high-performance Li-S battery. *Chem Eng J* 2020;381:122701. DOI

42. Zhang D, Kang Z, Liu X, Guo J, Yang Y. Highly sensitive ammonia sensor based on PSS doped ZIF-8-derived porous carbon/polyaniline hybrid film coated on quartz crystal microbalance. *Sens Actuators B Chem* 2022;357:131419. DOI
43. Nam S, Umrao S, Oh S, Shin KH, Park HS, Oh I. Sonochemical self-growth of functionalized titanium carbide nanorods on Ti_3C_2 nanosheets for high capacity anode for lithium-ion batteries. *Compos B Eng* 2020;181:107583. DOI
44. Lei D, Shang W, Zhang X, et al. Facile synthesis of heterostructured MoS_2-MoO_3 nanosheets with active electrocatalytic sites for high-performance lithium-sulfur batteries. *ACS Nano* 2021;15:20478-88. DOI
45. Hu S, Huang X, Zhang L, et al. Vacancy-defect topological insulators Bi_2Te_{3-x} embedded in N and B Co-doped 1D carbon nanorods using ionic liquid dopants for kinetics-enhanced Li-S batteries. *Adv Funct Materials* 2023;33:2214161. DOI
46. Li M, Yang D, Biendicho JJ, et al. Enhanced polysulfide conversion with highly conductive and electrocatalytic iodine-doped bismuth selenide nanosheets in lithium-sulfur batteries. *Adv Funct Materials* 2022;32:2200529. DOI
47. Huang T, Cao Q, Jing B, Wang X, Wang D, Liang L. Towards high-performance lithium-sulfur battery: Investigation on the capability of metalloid to regulate polysulfides. *Chem Eng J* 2022;430:132677. DOI
48. Gu Q, Qi Y, Chen J, Lu M, Zhang B. Cobalt nanoparticles loaded on MXene for Li-S batteries: Anchoring polysulfides and accelerating redox reactions. *Small* 2022;18:e2204005. DOI
49. Zhu Y, Deng Y, Chen G. Highly crinkled and interconnected N, O and S co-doped carbon nanosheet modified separators for efficient Li-S batteries. *Mater Chem Front* 2023;7:1072-81. DOI